A NOVEL METHODOLOGY FOR SHEAR COHESIVE LAW IDENTIFICATION OF BONDED REINFORCEMENTS

M. Perrella [1], **V. P. Berardi**[2], **G. Cricrì** [1]

[1] Department of Industrial Engineering, University of Salerno

via Giovanni Paolo II 132, 84084, Fisciano (SA), Italy

e-mail: mperrella@unisa.it, gcricri@unisa.it

[2]Department of Civil Engineering, University of Salerno

via Giovanni Paolo II 132, 84084, Fisciano (SA), Italy

e-mail: berardi@unisa.it

Abstract

Repair of structural elements with bonded fiber reinforced polymers (FRPs) is widely used in many engineering applications. Within the strengthening of civil structures, failure usually occurs due to FRP debonding by in-plane shear mode fracture. In this work, mode II fracture behavior of concrete specimens, reinforced with pultruded FRP, was investigated by the authors. Shear tests were performed by using both conventional equipment and a non-contact optical technique, Digital Image Correlation (DIC). Starting from the experimental data, the evaluation of the *J*-integral and of specimens' fracture toughness was carried out. Subsequently, a cohesive law was associated to the *J*-integral and thus identified by comparison with experimental data, by means of the theoretical approach proposed by Rice. The proposed cohesive zone (CZ)

model can be adopted in a Finite Element (FE) code for simulating the debonding failure in composite structures.

Keywords: A. Glass fibers; B. Debonding; C. Finite element analysis (FEA); CZM; *J*-integral; D. Mechanical testing; DIC.

1 INTRODUCTION

In recent years, adhesive bonding as joining technique has become frequent for structural purposes in many engineering fields, also as a consequence of the increasing use of composite materials. In mechanical engineering applications, bonded composites are typically used for the realization of industrial, automotive, naval and aerospace high-tech structural elements [1, 2]. Moreover, adhesive bonding is currently the most popular technique in repair and rehabilitation of existing civil structures (reinforced concrete and masonry structures), due to the development of innovative and cheaper FRP materials [3-6]. In particular, the use of FRPs provides the strengthening of structures subject to axial, flexural and shear loads and guarantees the reversibility of the intervention. This is an attractive aspect respect to conventional rehabilitation techniques, especially referring to historical buildings.

Although numerous are the advantages of strengthening by bonding composite plates and sheets, this method suffers from the uncertainty in estimating residual strength. No specific standards are required to be applied to the strengthening and construction of reinforced concrete and masonry civil structures until now, but some technical recommendations are provided in the American ACI 440.2R-08 [7], the European fib T.G. 9.3 [8] and the Italian CNR-DT 200 R1/2013 [9] guidelines. Within this context, some specific aspects of this technique have yet to be studied in deeper detail, like as the stress transfer mechanisms from composite to

strengthened member. These mechanisms depend on the specific type of junction: adhesive interface [10], anchorage device [11]. With reference to the adhesive junctions, it is well-known that their mechanical behavior can be modeled via a cohesive law, that allows also the prediction of the mode II fracture mechanism experimentally observed in failure of strengthened systems [12-13].

The identification of cohesive law requires the evaluation of relative displacements between FRP and structural element and FRP strains along the loading direction. The former are conventionally measured by means of either linear variable displacement transducers (LVDTs) or laser meter devices installed on composite plate and located at the beginning of bonded area. Whilst, the latter are commonly acquired through strain gauges, positioned along longitudinal direction [14-16].

Some recent studies have proposed a non-contact optical technique, DIC, to obtain relative displacements on extended areas of tested specimen rather than only on the beginning of bonded area [17-25]. This promising method also allows for an estimation, with a good accuracy, of the strain field on FRP and external surfaces of concrete core.

Such measuring method is prone to some problems, like the needs of a large amount of computer resources for mapping the strain field by DIC or the wide scatter of data.

A new and innovative methodology for the identification of cohesive law at the adhesive interface of strengthened systems is presented and validated in this work. The proposed approach is based on the *J*-integral formulation and DIC outcomes, without requiring any strain gages and LVDTs/laser meter records.

Experimental debonding tests on concrete blocks externally reinforced with GFRP pultruded laminates have been conducted for validation purposes by the authors at the Structural Engineering Testing Hall of the University of Salerno. Within experimental investigation, DIC method is applied only to selected regions of interest (ROI). This drastically reduces the

computational burden, pointing out experimental displacements in a more accurate way and overcoming the boundary effects of inhomogeneous zones.

A first validation of the proposed identification methodology has been performed by comparing the resulting predicted cohesive law with those obtained in a conventional way, i.e. starting from strain gauges records.

Further validation test has been done by comparing such a predictive cohesive law with that given by a direct identification scheme based on an accurate finite element model of the tested specimens (FEM virtual test).

2 EXPERIMENTAL ACTIVITY

Experimental characterization of adhesive interface of concrete reinforced with GFRP composite laminates is presented thereinafter. In detail, six samples were tested under quasi-static boundary conditions, according to the CNR-DT 200 R1/2013 guidelines.

Experimental tests were performed at the Structural Engineering Test Hall of the University of Salerno, using a universal servo hydraulic machine Schenck Hydropuls S56 equipped with a strain gauge data acquisition system (System 5000 by Vishay) and with a vision system (5 MPx CMOS camera sensor by IDS) for non-contact displacement measurements (Figure 1).

The specimens were constrained using a steel anchoring device mounted on the testing machine. The ends of the concrete block were clamped, whilst the composite laminate was gripped to the actuator for applying the loading condition, as suggested by the CNR-DT 200 R1/2013 guidelines.

Figure 1. Testing layout

Concrete blocks were fabricated using low strength concrete to best simulate the interface behavior of strengthened existing structures. Composite reinforcement was made of a pultruded E glass/polyester fiber reinforced polymer (E-glass fiber volume fraction equal to 35%). A two component epoxy resin Sikadur 30 by Sika was used for bonding.

The investigated typical specimen is shown in Figure 2.

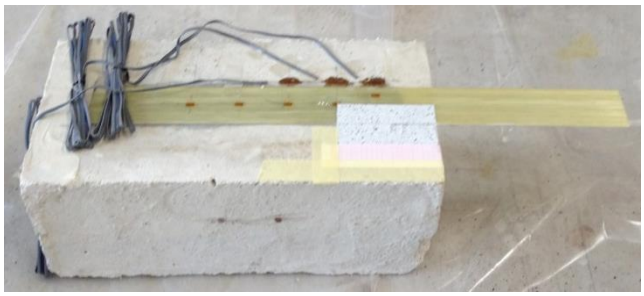

Figure 2. Details of a tested specimen

The specimens were realized using a GFRP pultruded laminate, whose total bonded length is 300 mm starting 50 mm from the front side of concrete block. No specific surface treatment

of concrete was adopted before bonding step. The specimens were cured at room temperature (21 °C) for 7 days. Concrete block and GFRP laminate dimensions are shown in Figure 3.

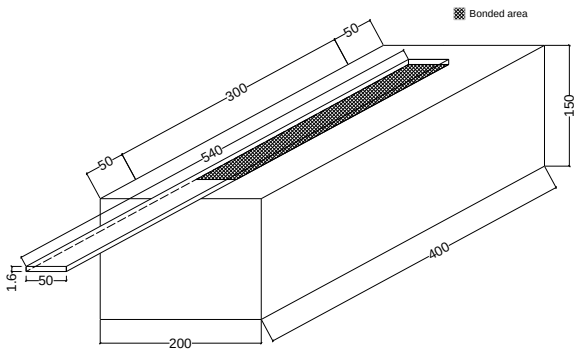

Figure 3. Geometry of the concrete blocks and the composite laminates [dimensions in mm]

First, six cubic samples of concrete (150x150x150 mm^3) were prepared and tested in order to evaluate the mean compressive strengths, respectively cubic R_{cm} and cylindrical f_{cm}. Second, tensile tests, according to ASTM D3039M standard, were performed to obtain the mean Young's modulus E_{GFRP} and ultimate tensile stress f_{GFRP} along fiber direction of the pultruded GFRP composite. The experimental mechanical properties of concrete and GFRP laminate, together with the nominal Young's modulus E_r and tensile strength f_r of resin Sikadur 30, as stated in the technical data sheet by manufacturer, are listed in Table 1.

Table 1. Mechanical properties of specimens' materials

R_{cm} [MPa]	f_{cm} [MPa]	E_{GFRP} [MPa]	f_{GFRP} [MPa]	E_r [MPa]	f_r [MPa]
19.09	15.84	48000	800	11200	25-30

Figure 4 shows the strain gauges configuration applied to each specimen, whilst their location along the loading direction x is specified in Table 2. The origin of x axis corresponds to the top edge of the bonded area.

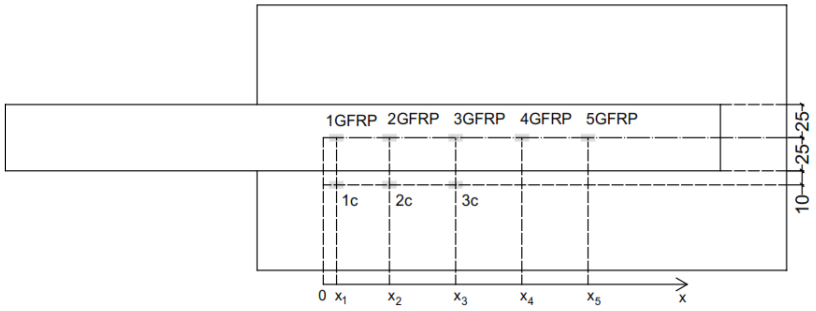

Figure 4. Position of the strain gauges applied to the specimens

The strain-gages location was modified for the specimens # 2-6, accounting for the response of specimen #1 testing, thus reducing the distance between consecutive sensors and removing unneedful strain gauges (i.e. the strain gauges 3c and 5GFRP).

Table 2. Strain gauges locations along the loading axis *x*

Test #	**x_1** [mm]	**x_2** [mm]	**x_3** [mm]	**x_4** [mm]	**x_5** [mm]
1	10	50	100	150	200
2-6	15	30	45	95	-

The tests were conducted under displacement control with a rate of 0.01 mm/s until the complete debonding occurred. The experimental data acquired during test execution are:

1) Digital video for image processing with DIC technique;
2) Relative displacement between specimen edges by the test machine (LVDT);
3) Load applied to composite laminate by the test machine load cell;
4) Strains of composite and concrete, measured via strain gauges.

The DIC technique was adopted for measuring the displacement field of the zone close to

the top interface edge, considering small (2 mm diameter) circular regions of interest (ROI) as in Figure 5.

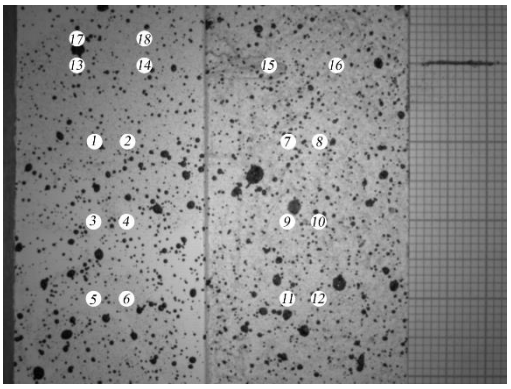

Figure 5. Position of the ROIs processed by DIC technique

The *Ncorr* algorithm [12], enhanced via an in house made Matlab routine, was used for DIC analysis. The resulting displacement vector for each ROI was obtained by getting the mean value of the computed data in the neighborhood of ROI center.

3 TEST RESULTS AND CONVENTIONAL IDENTIFICATION

The load-displacement curves, acquired by the testing machine during the debonding experiments, are plotted in Figure 6. The maximum values of the applied forces were observed within the range 12-14 kN, whereas the maximum displacement ranged within 1.5-2.5 mm.

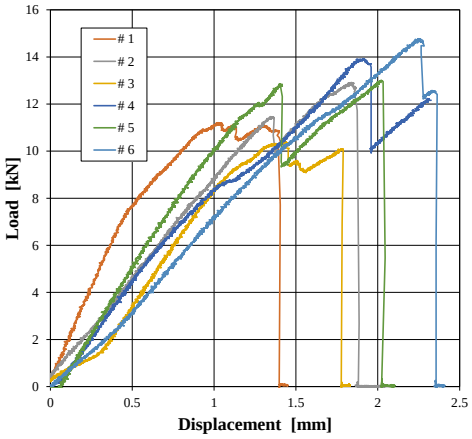

Figure 6. Testing machine load vs. displacement curves of all six specimens

In order to describe, in depth, the proposed identification methodology, the experimental results and the corresponding theoretical analysis are referred in the following to the specimen # 1, which exhibited a typical cohesive failure mode.

The fracture surface of the tested specimen # 1 is shown in Figure 7, where it is worth noting that the decohesion of the composite from the supporting block caused the removal of a thin layer of concrete.

Figure 7. Post mortem fracture surfaces of the specimen #1

The tangential slips $\delta_{i,i+1}$ evaluated by DIC technique, are considered as the relative displacement of mid points between the cross-sections corresponding to i-th and (i+1)-th GFRP strain gauges. The GFRP strain ε_i versus time curves and the tangential slip $\delta_{i,i+1}$ versus time curves are plotted for the specimen #1 in Figures 8 and 9, respectively.

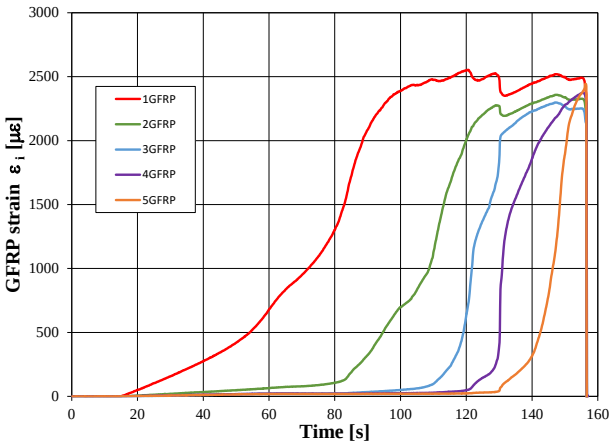

Figure 8. GFRP strain vs. time curves obtained by strain gauges records of specimen #1

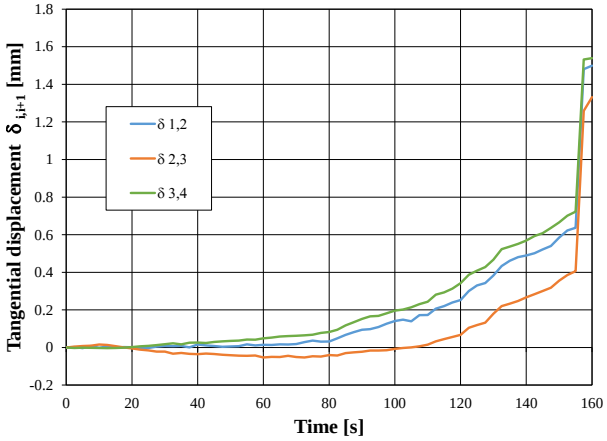

Figure 9. Tangential slip vs. time curves obtained by DIC technique for the specimen #1

The mean shear stresses at the adhesive interface, $\tau_{i,i+1}$, acting between the cross-sections corresponding to i-th and (i+1)-th GFRP strain gauges, can be evaluated by means of strains variation measured along the loading axis x, according to the method proposed in [9].

Specifically, let ε_i and ε_{i+1} be the acquired strains by two consecutive sensors (see Figure 4); the interface shear stresses can be calculated imposing the translational equilibrium condition for the composite small region included between the cross sections of the two considered strain gauges, located at x_i and x_{i+1}, respectively.

Thus, the mean shear stresses can be expressed as:

$$\tau_{i,i+1} = -\frac{E_{GFRP} \cdot A_{GFRP} \cdot (\varepsilon_{i+1} - \varepsilon_i)}{B_{GFRP} \cdot (x_{i+1} - x_i)} \quad (1)$$

$$A_{GFRP} = t_{GFRP} \cdot B_{GFRP}$$

where t_{GFRP}, B_{GFRP}, A_{GFRP} and E_{GFRP} are the thickness, the width, the cross sectional area and the Young's modulus along the fiber direction of the composite laminate, respectively.

The adopted method allows evaluating the mean shear stress distribution along x direction more accurately when the sensors are closer. The trend of mean shear stresses $\tau_{i,i+1}$ versus time of specimen # 1 are plotted in Figure 10. In particular, only the curves referred to the sensors far from the free edges of the bonded zone are reported in order to avoid edge effect errors.

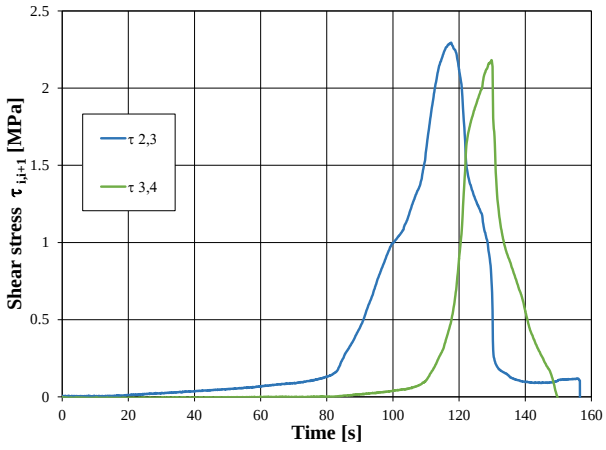

Figure 10. Shear stress vs. time curves of specimen #1

Using the time as parameter, the shear stress $\tau_{i,i+1}$ versus tangential slip $\delta_{i,i+1}$ curves are obtained (Figure 11).

These curves are representative of experimental evaluations of cohesive shear acting at the concrete-GFRP interface in a form coherent with a Cohesive Zone (CZM) approach and with recent literature results [14-25].

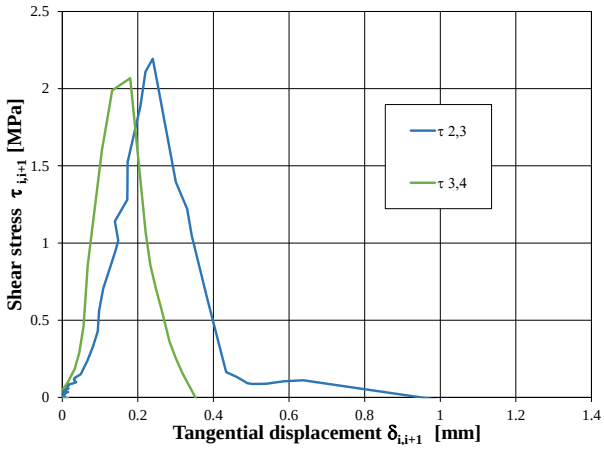

Figure 11. Shear stress vs. tangential slip curves of specimen #1

4 NEW IDENTIFICATION METHODOLOGY

The methodology is based on the well-known analytical relation existing between the cohesive tractions and the *J*-integral. From the experimental point of view, only the load output by testing machine and the displacements by DIC analysis are needed.

In details, let assume the following hypotheses: a) the concrete block is rigid, because of its negligible compliance if compared with that of the GFRP laminate, as also confirmed by the concrete strain gages records; b) the unbounded portion of the GFRP laminate is subject to pure axial load; c) the bonded interface carries pure shear load; d) the interface shear is constant over

the width of the GFRP laminate; e) the adherends behave as linear elastic.

Finally, the energy release rate, *G*, is expressed as:

$$G = \frac{P^2}{2 \cdot B_{GFRP}} \frac{dC(a)}{da} \tag{2}$$

being *P* the applied load, *a* the current crack length, *C* the compliance of the system.

Under the previous assumptions, the compliance *C* can be specialized as:

$$C(a) = \frac{w(a)}{P} = \frac{l(a)}{E_{GFRP} A_{GFRP}} = \frac{l_0 + a}{E_{GFRP} A_{GFRP}} \tag{3}$$

where *w*, *l* and l_0 are the longitudinal extension, the current length and the initial length of the unbounded portion of the GFRP laminate, respectively.

Starting from the well-known equality between the energy release rate *G* and the *J*-integral, *J*, which holds in the field of linear elasticity, and considering the equations (2) and (3), it is possible to obtain the following relationship:

$$J = G = \frac{P^2}{2 \cdot B_{GFRP} \cdot A_{GFRP} \cdot E_{GFRP}} = f(P) \tag{4}$$

With the aim of evaluating the interface cohesive law, it is useful to recall the analytical relationship between the *J*-integral and the cohesive traction that was pointed out by Rice [14].

In particular, for mode II (shear) load condition, it is:

$$\tau(\delta_s) = \frac{\partial J(\delta_s)}{\partial \delta_s} \tag{5}$$

where τ is the cohesive shear stress and δ_s is the tangential slip separation measured at the crack tip.

In the present approach, the slip displacement δ_s was evaluated as follows. Four small circular regions of interest were defined for the DIC processing: two located on the GFRP laminate and the remaining on the concrete block; further, the ROIs were preferably chosen aligned orthogonally with respect to the loading axis. Following the numbering and the symbols depicted in Figure 12, let indicate the ROIs centers' displacements along the loading axis with $u_1 \ldots u_4$; then, the slip displacement is given by:

$$\delta_s = u_2 - u_3 + \frac{s_1}{d_{12}}(u_2 - u_1) + \frac{s_2}{d_{34}}(u_4 - u_3) \tag{6}$$

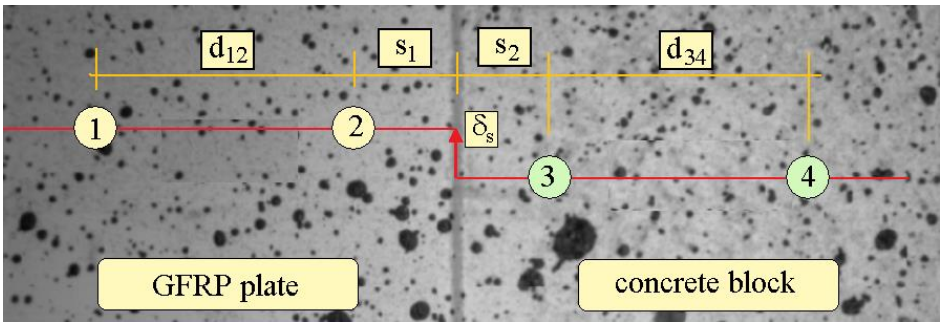

Figure 12. Scheme of ROIs' location for tangential slip displacement evaluation

Note that the slip displacement calculated by formula (6) accounts for any small rigid in-plane rotations of adherends. If failure occurs in pure mode II, as expected from debonding test, possible rotations of adherends are the same. Thus, the relationship (6) eliminates the possible error due to the rigid rotation of the test specimen with respect to camera.

The equation (5) is sufficient, from a theoretical point of view, for predicting the cohesive

law $\tau(\delta_s)$ by finite increments, since *J* can be evaluated from the testing machine load cell data using equation (4), and δ_s by the DIC outcomes using equation (6). Nevertheless, it is convenient to define some analytical models of $\tau(\delta_s)$ for regularizing the experimental outcomes and make the cohesive law useful within further numerical or analytical analyses.

In the present work, the cohesive shear stress behavior was modeled with an exponential law, firstly introduced by Xu and Needleman [13] for the mixed mode cohesive tractions. The expression of this law, particularized for the mode II condition, is:

$$\tau(\delta_s) = \sqrt{2e}\tau_{max}\left(\frac{\delta_s}{\delta_{sc}}\right)e^{-\left(\frac{\delta_s}{\delta_{sc}}\right)^2} \quad (7)$$

where τ_{max} is the maximum shear stress carried by the interface, δ_{sc} is the scale factor of the tangential slip and *e* is the Neper number.

Differently from the methodologies proposed in literature [14-24], the experimental data were fitted with equation (4) instead of equation (7).

More specifically, such a fitting allowed to deal with an easily differentiable function *J* for obtaining the derivative $\tau(\delta_s)$, thus avoiding the unsmoothness resulting from a direct numerical derivative operation of the *J*-integral calculated by experimental set of data. For this reason, the integral form of equation (7) was calculated, under the assumption that *J* is zero at the initial time instant, as follows:

$$J(\delta_s) = \int_0^{\delta_s}\tau(x)dx = J_c\left(1 - e^{-\left(\frac{\delta_s}{\delta_{sc}}\right)^2}\right) = g(\delta_s; J_c, \delta_{sc}) \quad (8)$$

where J_c is the critical (maximum) value of the *J*-integral and δ_{sc} is the tangential slip distance

corresponding to the occurrence of maximum cohesive shear stress. From the fracture toughness evaluation, the following relation holds:

$$\sqrt{2e}\tau_{max}\delta_{sc} = 2J_c. \tag{9}$$

The parameters J_c and δ_{sc} were estimated following the strategy described below.

Firstly, J_c was calculated by the formula (4), as follows:

$$J_c = \frac{P_c^2}{2 \cdot \mathrm{B}_{GFRP} \cdot \mathrm{A}_{GFRP} \cdot \mathrm{E}_{GFRP}} \tag{10}$$

where P_c is the *plateau* load, estimated from the experimental data.

The scale parameter δ_{sc} was predicted by solving the following minimization problem, where the set of the *k* data corresponding to the early stage of the test was used (see Figure 13):

$$\min_{\delta_{sc}} \sum_k \left(g(\delta_{sk}; \delta_{sc}, J_c) - f(P_k)\right)^2 \tag{11}$$

The function $g(\delta_{sk}; \delta_{sc}, J_c)$ was obtained by the equation (8), whereas $f(P_k)$ was calculated by equation (4). The good agreement between the data points $f(P_k)$ of specimen #1 and the fitting curve (8) is highlighted in Figure 13.

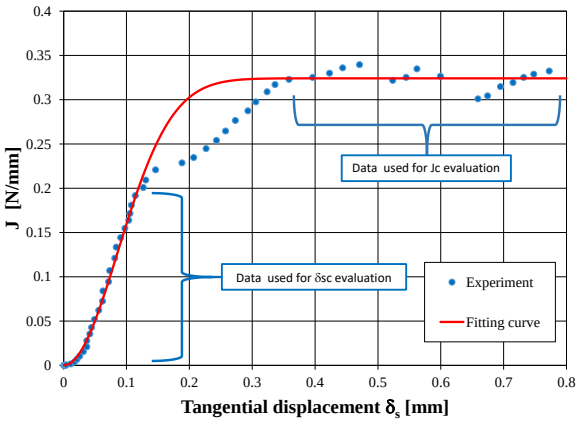

Figure 13. Experimental and analytical *J*-integral vs. tangential displacement curves

The values of the CZM parameters resulting from the proposed identification procedure are listed in Table 3. In the same table, the J_c and τ_{max} evaluations from the shear-tangential slip curves, calculated in the previous section and shown in Figure 11, are also reported for comparison. Finally, the shear-tangential slip curve derived by the proposed methodology is depicted in Figure 14 and compared with those obtained with conventional technique.

Table 3. CZM parameters from new methodology and conventional identification

	J_c [N/mm]	δ_{s_c} [mm]	τ_{max} [N/mm^2]
CZM parameters (new methodology)	0.3241	0.1214	2.290
Curve $\tau_{2,3} - \delta_{2,3}$ (conventional identification)	0.40		2.20
Curve $\tau_{3,4} - \delta_{3,4}$ (conventional identification)	0.23		2.10

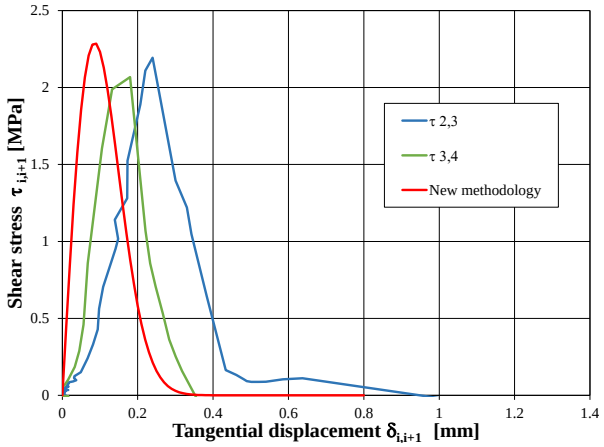

Figure 14. Comparison of shear stress vs. tangential slip separation curves

It is worth noting that a non negligible scatter among the shear curves is pointed out. This is further evidenced by comparing the values of the fracture toughness J_c reported in Table 3, which ranges from about 0.20 to 0.40 N/mm.

Let's note that the proposed novel methodology has exhibited, with respect to the most used approaches available in literature, a significantly lower computational and time burden, due to the optimization of DIC technique by limiting the analysis to proper regions of interest and to the calibration of CZM parameters based on the *J*-integral curve.

5 NEW METHODOLOGY VALIDATION

With the aim to validate the proposed methodology, an independent and direct CZM identification, based on the experimental outcomes of sample #1, was carried out according to the approach described in [6, 29].

More specifically, an accurate FE model of the test specimen was firstly implemented, assuming the CZM given by equation (7) and the constraint defined in the equation (9). The search of the unknown CZM parameters τ_{max}, δ_{sc}, J_c, was successively performed via an iterative

FEM analysis, resulting in a virtual load-displacement curve close to the experimental one.

From a computational point of view, the test specimen was discretized with about 150000 solid and 5000 interface elements, within a nonlinear analysis via the ANSYS code. The FE model is depicted in Figure 14.

Such an approach is expected to provide more precise results than the previous methods, because it uses only the testing machine load and displacement outputs, which are in general less prone to experimental errors, and it takes the tridimensional effects into account. For these reasons, its outcomes were used as a benchmark in this work.

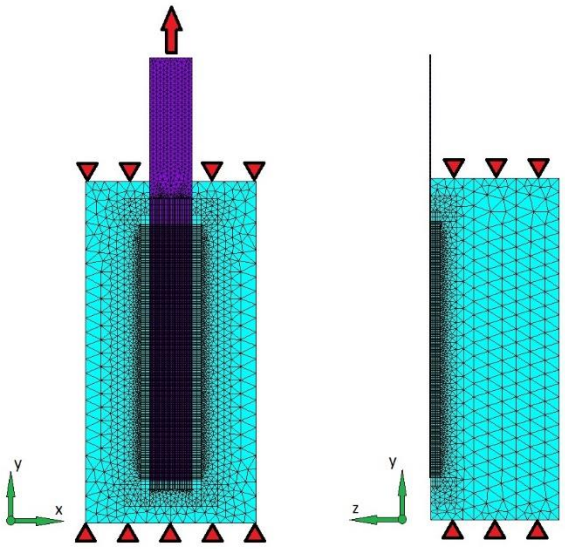

Figure 14. FE model used for the CZM direct identification

The comparison between the simulated and the experimental load-displacement curves was performed by using two parameters that characterize the global behavior of the experimental curve: the initial slope k_0 and the critical load P_c.

Since the independent CZM parameters to be set are two, the direct identification requires the solution of a nonlinear system that has two equations and two unknowns. For the sake of

convergence speed, the parameters δ_{sc} and J_c, were chosen as unknowns. In detail, indicating the FE analysis outcomes with the subscript "*FE*" and the experimental targets with the subscript "*T*" the identification results δ_{sc} and J_c come out from the solution of the following system of equations:

$$\begin{cases} k_{0FE}(\delta_{sc}, J_c) = k_{0T} \\ P_{cFE}(\delta_{sc}, J_c) = P_{cT} \end{cases} \tag{11}$$

The target values of k_0 and P_c, coming from the experimental data, are:

k_{0T} = 15.64 kNmm^{-1};

P_{cT} = 10.76 kN.

The equation (11) was solved via Newton-Raphson iterative algorithm, and the convergence criterion was set at 0.001 for each unknown. After few simulation runs, a convergent solution was attained, whose corresponding values of the CZM parameters are reported in Table 4, in comparison with the new methodology outcomes.

Table 4. CZM parameters resulting from new methodology and direct identification

	J_c [N/mm]	δ_{s_c} [mm]	τ_{max} [N/mm^2]
J-integral identification (new methodology)	0.3241	0.1214	2.290
Direct identification (FEM virtual test)	0.302	0.120	2.160
Percentage difference	-7.3%	-1.1%	-6.0%

In Figure 15, the experimental and simulated load-displacement curves are plotted for

comparison.

The *J*-integral based methodology has provided results very close to the ones based on the direct identification. Indeed, the proposed methodology has slightly underestimated the CZM parameters by few percent points with respect to the more precise and detailed direct identification (see Table 4). The underestimation can be mainly explained considering that, differently from the FE model solution, in equation (4) the concrete contribution to the elastic energy is neglected.

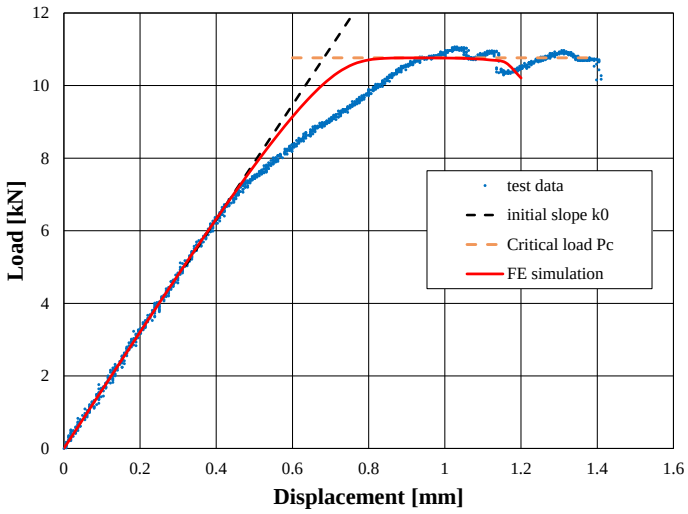

Figure 15. Experimental and simulated load vs. displacement curves

The FE convergent simulation also gives further information about the effectiveness of the proposed methodology for the identification of a cohesive law.

The stress along the load direction, σ_y, are reported in Figure 16 at growing steps of the simulation. Taking advantage of the symmetry, only half model is represented in the frontal view of specimen. The first stress map (on the left) is referred to the first debonding advance and the last one (on the right) to the end of the stable phase of the debonding growth.

These results also highlight that the longitudinal stresses in the concrete block are negligible

with respect to those in the GFRP laminate and, then, they are in line with the assumption above introduced about the rigid behavior of the concrete block.

The shear stresses, τ_{zy}, evaluated at the same steps of the normal stress σ_y, are reported in Figure 17. Let's note that the zone with higher stress values (in red), as expected, follows the debonding front; differently from the longitudinal stress, the shear stress values in the concrete and in GFRP exhibit the same order of magnitude; the maximum shear stresses in the adherends correspond to the CZM parameter τ_{max} (*i.e.* 2.16 MPa).

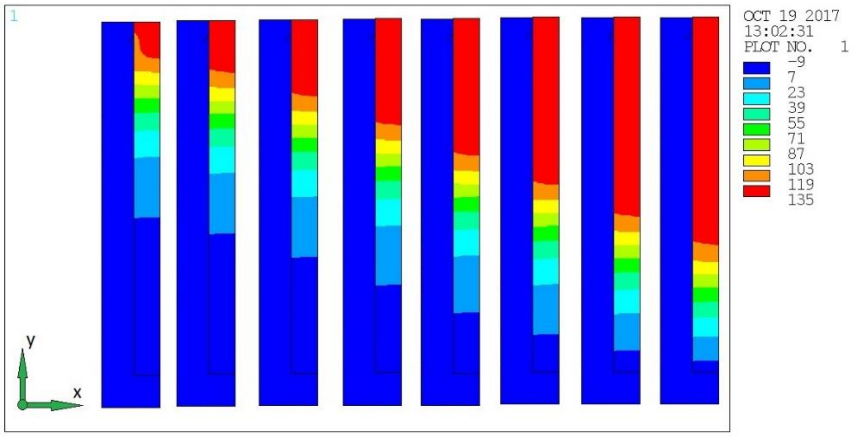

Figure 16. Sequence over time of the σ_y stress field [MPa] (frontal view of half model)

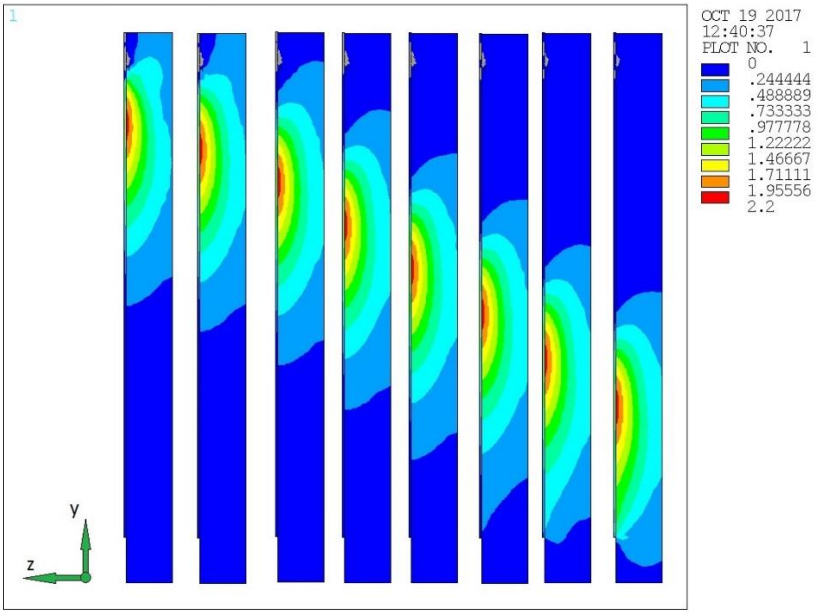

Figure 17. Sequence over time of the τ_{zy} stress field [MPa] (section at the symmetry plane)

The response of the interface elements is reported, in more details, in Figures 18 and 19. In particular, the shear stresses τ_{II}, τ_{III} and the normal stress σ_n of the interface elements at a given representative time are sequentially reported in Figure 18. The corresponding shear slips δ_{II}, δ_{III} and the opening separation δ_n are reported in Figure 19.

The examination of these results allows one to conclude that both the opening stress/jump displacement (mode I) and the shear/slip parallel to the debonding front (mode III) are negligible with respect to the shear/slip orthogonal to the crack front (mode II). Further, the prevalent shear/slip distribution (reported into the first frames of Figures 18-19) shows that the interface shear is essentially constant over the width of the GFRP laminate.

The above remarks point out that all the hypotheses of the proposed methodology for the identification of a cohesive law are well justified for the considered testing layout.

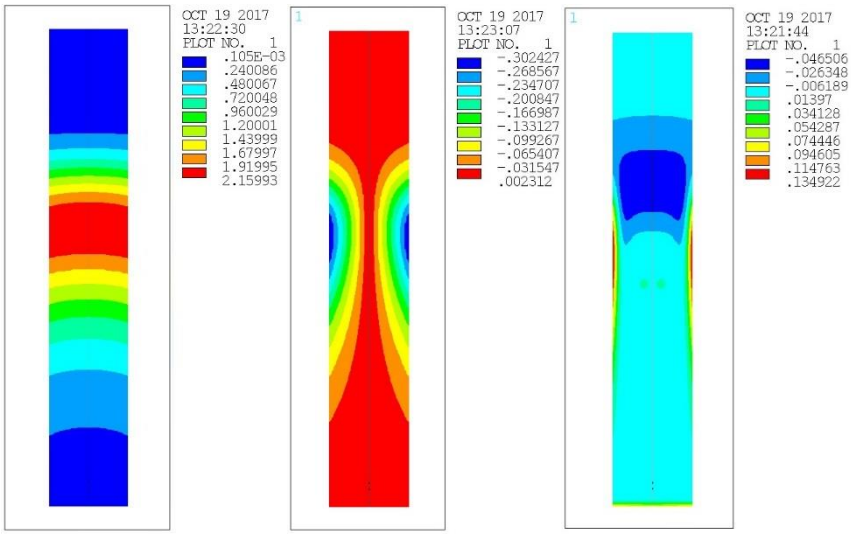

Figure 18. Interface stress (τ_{II}, τ_{III}, σ_n) of cohesive elements from virtual test [MPa]

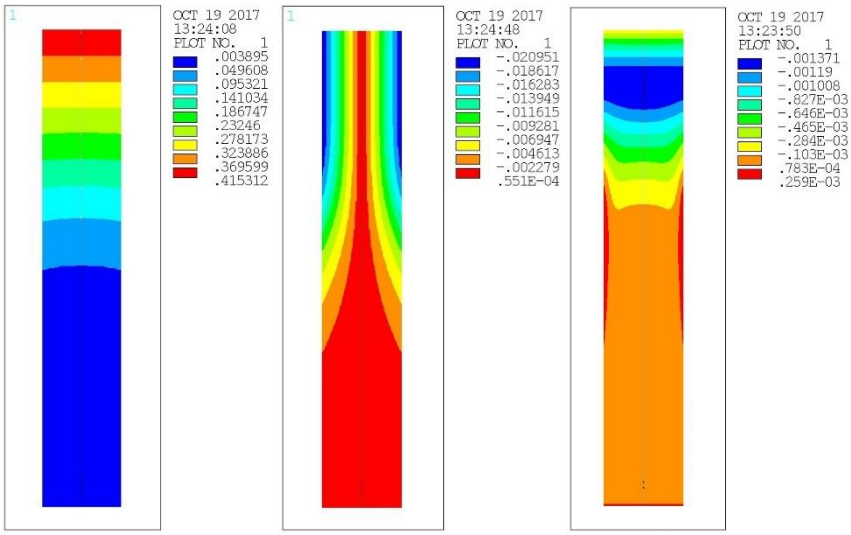

Figure 19. Interface separation (δ_{II}, δ_{III}, δ_n) of cohesive elements from virtual test [mm]

6 CONCLUSIONS

A new and smart methodology for the theoretical-experimental identification of a cohesive law was proposed in this paper, in the field of strengthening with externally bonded reinforcement of existing structures. The presented approach allows to model the interface behavior between the adherends via few experimental data and *J*-integral evaluation. The experimental data were provided by testing machine load cell and DIC technique, applied to proper regions of interest.

The methodology was applied and validated within an experimental investigation of the debonding failure of concrete blocks reinforced with GFRP pultruded laminates. The tests were carried out at the Structural Engineering Testing Hall of the University of Salerno by using both conventional equipment and DIC method.

This non-contact optical technique has allowed to reach a good accuracy of the full field displacement measurement and to overcome the limits of the conventional acquiring by LVDT or laser measurement devices, which provide displacements only in correspondence of sensor positions.

The behavior of investigated adhesive layer, undergoing mode II failure, was studied by means of Rice's theory that correlates the cohesive tractions with *J*-integral approach.

Cohesive stresses resulting from the proposed methodology were compared with those obtained using conventional approach, based on strain gages records. The comparison is satisfactory in terms of maximum shear stress, whilst the fracture toughness evaluation exhibits a not negligible scatter.

The validation of the proposed methodology was performed through an accurate 3D FEM analysis of the debonding test. This virtual test was used for obtaining an independent direct identification of cohesive law based on the testing machine load-displacement curve. The outcomes of virtual test validated the assumed hypotheses of the proposed methodology.

A sound agreement between the results obtained by the analytical cohesive law and that given by FEM analysis was observed, in terms of both maximum shear stress and fracture toughness.

The abovementioned comparisons has highlighted the reliability of the proposed methodology, against a limited computational and time burden, due to the optimized use of DIC technique, the choice of suitable experimental targets for the calibration of CZM parameters.

In a near future, we address extensions of the methodology proposed in this work to the modeling of the long-term behavior of adhesive interface, accounting its viscous nature [30, 34].

REFERENCES

[1] R. Citarella, G. Cricrì, Three-dimensional BEM and FEM submodelling in a cracked FML full scale aeronautic panel. *Applied Composite Materials*, **21 (3)**, 557-577, 2014.

[2] V. Corato, L.Affinito, A. Anemona, U. Besi Vetrella, A. della Corte, A. Di Zenobio, C. Fiamozzi Zignani, R. Freda, G. Messina, L. Muzzi, M. Perrella, L. Reccia, G. Tomassetti, S. Turtù, Detailed design of the large-bore 8T superconducting magnet for the NAFASSY test facility. *Superconductor Science and Technology*, **28(3)**, art. no. 034005, 2015.

[3] H.R. Ronagh, A. Eslami, Flexural retrofitting of RC buildings using GFRP/CFRP - A comparative study. *Composites Part B: Engineering*, **46**, 188-196, 2013.

[4] D'Ambrisi, A., Mezzi, M., Feo, L., Berardi, V.P., Analysis of masonry structures strengthened with polymeric net reinforced cementitious matrix materials. *Composite Structures,***113 (1)**, 264-271, 2014.

[5] F. Fabbrocino, I. Farina, V.P. Berardi, A.J.M. Ferreira, F. Fraternali, On the thrust surface of unreinforced and FRP-/FRCM-reinforced masonry domes. *Composites Part B: Engineering*, **83**, 297-305, 2015.

[6] G. Cricrì, M. Perrella, Investigation of mode III fracture behaviour in bonded pultruded GFRP composite joints.*Composites Part B: Engineering*, **112**, 176-184, 2017.

[7] American Concrete Institute (ACI). Guide for the design and construction of externally bonded FRP systems for strengthening concrete structures. ACI 440.2R-08, Farmington Hills, MI, 2008.

[8] Fib TG 9.3, Technical report on the "Design and use of externally bonded fibre reinforced polymer reinforcement (FRP EBR) for reinforced concrete structures", 1-138, 2001, ISBN 2-88394-054-1.

[9] National Research Council of Italy, Guide for the Design and Construction of Externally Bonded FRP Systems for Strengthening Existing Structures - CNR-DT 200R1-2013. Advisory Committee on Technical Regulations for Constructions, Rome, 2013.

[10] L. Ascione, V.P. Berardi, L. Feo, G. Mancusi, A numerical evaluation of the inter-laminar stress state in externally FRP plated RC beams. *Composites Part B: Engineering*, **36(1)**, 83-90, 2005.

[11] L. Ascione, V.P. Berardi, Anchorage device for FRP laminates in the strengthening of concrete structures close to beam-column joints. *Composites Part B: Engineering*, **42 (7)**, 1840-1850, 2011.

[12] G. Mancusi, F. Ascione, Performance at collapse of adhesive bonding. *Composite Structures*, **96**, 256-261, 2013.

[13] A. Orefice, G. Mancusi, L. Feo, F. Fraternali, Cohesive interface behaviour and local shear strains in axially loaded composite annular tubes. *Composite Structures*, **160**, 1126-1135, 2017.

[14] C. Mazzotti, M. Savoia, B. Ferracuti, A new single-shear set-up for stable debonding of FRP–concrete joints. *Construction and Building Materials*,**23**, 1529–1537, 2009.

[15] F. Bencardino, A. Condello, A.F. Ashour, Single-lap shear bond tests on Steel Reinforced Geopolymeric Matrix-concrete joints. *Composites Part B: Engineering*, **110**, 62-71, 2017.

[16] S. De Santis, F. Ceroni, G. de Felice, M. Fagone, B. Ghiassi, A.Kwiecień, G.P. Lignola, M. Morganti, M. Santandrea, M. R. Valluzzi, A. Viskovic. Round Robin Test on tensile and bond behaviour of Steel Reinforced Grout systems. *Composites Part B: Engineering*, **127**, 100-120, 2017.

[17] M. Ali-Ahmad, K. Subramaniam, M. Ghosn, Experimental investigation and fracture analysis of debonding between concrete and FRP sheets. *Journal of Engineering Mechanics*, **132 (9)**, 914-923, 2006.

[18] C. Carloni, K.V.Subramaniam, Direct determination of cohesive stress transfer during debonding of FRP from concrete. *Composite Structures*, **93 (1)**, 184-192, 2010.

[19] F.G. Carozzi, P. Colombi, C. Poggi, Calibration of end-debonding strength model for FRP-reinforced masonry. *Composite Structures*, **120**, 366-377, 2015.

[20] A. Napoli, G. de Felice, S. De Santis, R.Realfonzo, Bond behaviour of Steel Reinforced Polymer strengthening systems. *Composite Structures*, **152**, 499-515, 2016.

[21] C. Carloni, M. Santandrea, I. A. O. Imohamed, Determination of the interfacial properties of SRP strips bonded to concrete and comparison between single-lap and notched beam tests. *Engineering Fracture Mechanics*, **186**, 80-104, 2017.

[22] D.A. Pohoryles, J. Melo, T. Rossetto, M. Fabian, C. McCague, K. Stavrianaki, B. Lishman, B. Sargeant, Use of DIC and AE for Monitoring Effective Strain and Debonding in FRP and FRCM-Retrofitted RC Beams. *Journal of Composites for Construction*, **21 (1)**, 2017.

[23] M. Ghorbani, D. Mostofinejad, A. Hosseini, Bond Behavior of CFRP Sheets Attached to Concrete through EBR and EBROG Joints Subject to Mixed-Mode I/II Loading. *Journal of Composites for Construction*, **21 (5)**, 2017.

[24] A. Bilotta, F. Ceroni, G.P. Lignola, A. Prota, Use of DIC technique for investigating the behaviour of FRCM materials for strengthening masonry elements. *Composites Part B: Engineering*, **129**, 251-270, 2017.

[25] M. Tekieli, S. De Santis, G. de Felice, A. Kwiecien´, F.Roscini, Application of Digital Image Correlation to composite reinforcements testing. *Composite Structures*, **160**, 670-688, 2017.

[26] J. Babler, B. Adair, A. Antoniou, Ncorr: Open-Source 2d Digital Image Correlation Matlab Software, *Experimental Mechanics*, **55**, 1105-1122, 2015.

[27] X-P Xu, A. Needleman, Numerical simulations of fast crack growth in brittle solids. *Journal of the Mechanics and Physics of Solids*, **42**, 1397-1434, 1994.

[28] J.R.Rice, A path independent integral and the approximate analysis of strain concentrations by notches and cracks. *J Appl Mech*, **35**, 379-86, 1968.

[29] N. Valoroso, S. Sessa, M. Lepore, G. Cricrì, Identification of mode-I cohesive parameters for bonded interfaces based on DCB test. *Engineering Fracture Mechanics*, **104**, 56-79, 2013.

[30] C. Calì, G. Cricrì, M. Perrella, An Advanced Creep Model for Hardening and Damage Effects. *Strain*, **46**, 347–357, 2010.

[31] L.Ascione, V.P. Berardi, A. D'Aponte, A viscoelastic constitutive law for FRP materials. *International Journal of Computational Methods in Engineering Science and Mechanics*, **12 (5)**, 225-232, 2011.

[32] L. Ascione, V.P. Berardi, A. D'Aponte, Creep phenomena in FRP materials. *Mechanics Research Communications*, **43**, 15-21, 2012.

[33] G. Mancusi, S. Spadea, V. P. Berardi, Experimental analysis on the time-dependent bonding of FRP laminates under sustained loads. *Composites Part B: Engineering*, **46**, 116-122, 2013.

[34] V. P. Berardi, M. Perrella, L. Feo, G. Cricrì, Creep behavior of GFRP laminates and their phases: Experimental investigation and analytical modelling. *Composites Part B: Engineering*, **122**,136-144, 2017.